Alexandria Engineering Journal 99 (2024) 394–407

Contents lists available at ScienceDirect

Alexandria Engineering Journal

journal homepage: www.elsevier.com/locate/aej

Machinability of extruded H13 tool steel: Effect of cutting parameters on cutting forces, surface roughness, microstructure, and residual stresses

Stepan Kolomy [a], Martin Maly [a,b,*], Josef Sedlak [a], Jan Zouhar [a], Martin Slany [a], Pavel Hrabec [a], Karel Kouril [a]

[a] Institute of Manufacturing Technology, Faculty of Mechanical Engineering, Brno University of Technology, Technicka 2896/2, Brno 616 69, Czech Republic
[b] Central European Institute of Technology (CEITEC), Brno University of Technology, Purkynova 656/123, Brno 612 00, Czech Republic

ARTICLE INFO

Keywords:
H13 tool steel
Material extrusion
Cutting forces
Microstructure
Microhardness
Residual stresses

ABSTRACT

The production of H13 tool steel (TS) by material extrusion (MEX) is a promising method in various applications, but as-built surface roughness does not comply with the quality requirements. Hence, this study investigated the effects of cutting parameters on tool wear, cutting forces, surface quality, microhardness, structure, and residual stresses when machining H13 TS produced by MEX. Dry machining (DM) proved advantageous in certain indicators such as tool wear and cutting forces in comparison to the flood cooling (FC). The lowest surface roughness (0.08 μm) was achieved at the cutting speed of 80 m/min, feed per tooth of 0.005 mm, and FC which corresponded to a 41 % decrease compared to DM under same conditions. Surface microhardness increased by 20 % after machining, decreasing with distance from the surface. The highest compressive residual stresses were observed under FC, while the DM resulted in a 78.2 % decrease in residual stresses due to a partial annealing effect caused by higher surface temperature. Overall, DM exhibited great potential for achieving high-quality surfaces with a favorable structure and residual stresses. This study's novelty and robustness lie in its significant contribution to practical industrial applications, such as mold and core production.

1. Introduction

Recently, additive manufacturing (AM) has been developed from an experimental, prototype-manufacturing method to an approved manufacturing technology to produce more advanced pieces [1]. The powder bed fusion technology is a very popular method for creating these parts, which provides a chance to design parts with high resolution and good mechanical properties [1,2]. However, there are also other technologies, for example, direct energy deposition (DED), binder jetting (BJT), or material extrusion (MEX [3,4]which can produce various metal materials, such as steels [5] or PLA plastic materials [6]. MEX exhibits a great potential to replace other AM technologies (such as DED and BJT) in some applications [7]. The principle of MEX is similar to conventional injection molding and can be explained as a multi-step process (3D printing, debinding, and sintering) [8].

MEX is carried out by an extrusion nozzle through which the feedstock is extruded layer by layer. Process parameters, such as the number of perimeters [9], 3D printing temperature [10], scanning speed [11], flow rate [12] and so on, can influence the final mechanical properties of the part. It is advisable to keep the temperature of the build platform lower than the temperature of the glass transition of the binder in the raw material. MEX uses a build sheet between the part and the build platform to increase adhesion and prevent the part from warping [13]. The part after the 3D printing is called the green body and afterward a debinding process follows which removes the binder from the green body by washing it for at least 48 hours in a solvent bath [14]. By using debinding technologies, such as thermal, solvent, and catalytic methods, a brown body is created [15]. Sintering is the last step of the AM process, which removes the rest of the binder. The final part is acquired by the sintering process with subsequent cooling which is carried out in the furnace under a protective atmosphere to prevent the oxidation of the sintered part [16]. The atmosphere in the furnace during sintering is a crucial factor that affects the final properties of the piece. Singh et al. [17] found out that the hardness, relative density, and ultimate tensile strength were lower in the sample produced by MEX than the wrought one due to such internal porous defects.

* Corresponding author at: Institute of Manufacturing Technology, Faculty of Mechanical Engineering, Brno University of Technology, Technicka 2896/2, Brno 616 69, Czech Republic.
E-mail address: maly@vutbr.cz (M. Maly).

https://doi.org/10.1016/j.aej.2024.05.018
Received 16 November 2023; Received in revised form 30 April 2024; Accepted 4 May 2024
Available online 19 May 2024

MEX, also known as bound metal deposition (BMD) or atomic diffusion additive manufacturing (ADAM), is a promising method for creating parts in various applications, including molds for injection molding. Moreover, MEX offers several advantages which can be drawn as follows. MEX can produce a mold with complex geometries and conformal cooling channels that are difficult or impossible to create by traditional manufacturing methods. MEX can reduce the cost of mold, especially for small-batch production. MEX enables to manufacture a mold in a fraction of the time required for traditional manufacturing methods, such as CNC machining [18].

The H13 TS is widely used for wear-resistant pieces, such as injection molds exposed to a high working temperature and fatigue. Using AM to produce an injection mold can provide better cooling channels with complex shapes, but an appropriate post-processing operation by machining must be performed. Surface quality can be improved by machining and subsequent rolling [19]. In addition, better surface quality can increase fatigue performance as discussed by Opela et al. [20]. There are a few studies concerning the evaluation of the machinability of H13 TS when turning [21,22,23]. Mahapatra et al. [24] aim to analyze the tool vibration, surface roughness, and chip morphology when hard turning of H13 TS with minimum quantity lubrication. They confirm that the nose radius contributes the most to surface roughness while the cutting speed most affects the tool vibration. Kumar et al. [25] focus on analyzing the impacts of three distinct grades of CBN inserts with respect to both cutting forces and surface roughness when hard turning H13 TS. They find out that the surface roughness decreases with the higher hardness of the workpiece and increases with a higher feed rate. The investigation of milling H13 TS was the aim of Cicek et al. They investigate the wear of coated tungsten carbide end mills [26] and HSS end mills [27] when machining wrought H13 TS. They find out that under wet cutting conditions, the Ra values exhibit notable improvements, primarily attributable to the cooling and lubricating effects provided by the cutting fluid. Montevecchi et al. [28] use laser deposition and wire-arc additive manufacturing for building samples to investigate the machinability of H13 TS when compared with the same material in the wrought state. In summary, this study draws attention to the increased difficulty of machining H13 produced by AM compared to its wrought state counterpart. The findings reveal a notable rise in cutting forces and cutting force coefficients during the machining process [28].

Due to a shortage or even nonexistence of studies focused on machinability of H13 TS produced by MEX and the undisputed potential of this production method, the purpose of the current study is to fill the research gap by the following investigation. The novelty of the paper is an examination of the effect of cutting conditions (cutting speed, feed per tooth, and cooling) on the machinability of H13 TS produced by MEX. The full factorial design of the experiment was used for the testing, where the parameters, such as the final surface roughness, cutting forces, tool wear, microhardness, structures, and residual stresses, were evaluated. The parameters of surface roughness and cutting forces were investigated by regression analysis, which provides a good chance to predict these aspects during the machining.

2. Experimental procedure

2.1. Sample preparation

H13 TS metal feedstocks served for the fabrication of the samples. The chemical composition of H13 TS is depicted in Table 1. The rods used for fabrication consisted of metal, wax, and polymer, which are used as binders during the building process. The as-designed block samples were produced by MEX (the principle of this method is depicted in Fig. 1a). The total of three metal test blocks (60×30×20 mm, see Fig. 1b), named A, B, and C, were built by an alternating line strategy, which fabricates the samples according to the pattern depicted in Fig. 1c. The direction of 3D printing was characterized by the z-direction and used process parameters are listed in Table 2. The 3D printer consists of two extrusion nozzles; the first is for 3D printing of the feedstock, and the second for 3D printing of the ceramic material which is used as a build sheet for easier part removal from the build platform.

The samples were 3D printed by a commercially available device created via the Desktop Metal company which is called Studio System. The whole system consists of the 3D printer, the debinding device, and the sintering furnace. The H13 TS metal samples were 3D printed by a 400-μm-diameter extrusion nozzle at a temperature of 175 °C, while the build platform was preheated at 65 °C. The extrusion nozzle used for the ceramic building featured the same diameter and the build chamber was closed and heated up to 50 °C.

The debinding process, which lasts 252 h, was separated into two steps. In the first step (solvent debinding step), the parts were immersed in the debinding fluid. During the first step, the fluid temperature reached 44 °C. During the drying step (the second step), the processing tank temperatures increased to 70 °C. The sintering cycle was held under pure argon atmosphere according to conditions developed by Desktop Metal, with a recommended sintering cycle time of 41 h.

2.2. Machinability of the material and settings

The testing of the machinability was carried out using the solid carbide end mills with the TiN applied coating, which should be able to machine the material with the maximum hardness of 60 HRC (the tested samples featured a hardness of 47.5 ± 5 HRC in as-sintered state). There are several parameters which can affect the machinability of the material, i.e., workpiece material (especially the mechanical properties), cutting conditions, clamping, cooling, etc. The conditions which were constant during the whole experiment are shown in Table 3. The tool wear at the end of the test was evaluated with the Zeiss Stemi 2000-C optical microscope.

The main aim was to evaluate the effect of the cutting conditions, namely cutting speed v_c, feed per tooth f_z, and cooling conditions, i.e., DM and FC on the machinability of the samples. The tests of material machinability were performed according to the full factorial design of experiment (DoE) with repeated measurement in the central point procedure, which was prepared with the Minitab 21.4 software. Runs of experiments were randomized to avoid confounding DoE factors with time. Furthermore, the machined distance was considered as a covariate for this experiment. The DoE procedure is depicted in Table 4 which shows twelve individual tests marked in ranges I to XII (the visualization is also included). Each sample (A, B, C) was used for the four individual tests of the machinability. The methodology of the testing is depicted in Fig. 2a and the sample clamping in Fig. 2b respectively.

2.3. Evaluation of the material machinability

Each test listed in Table 4 was subjected to the cutting forces measurement (F), microhardness evaluation (M), structure observation (S), and quality examination (Q). The regions where the analyses were carried out concerning each sample are depicted in Fig. 2a. The cutting forces (F) were measured in regions marked 1–7 using the Kistler dynamometer, which can examine the forces in the three-perpendicular

Table 1
Chemical composition of the H13 TS metal rods.

Elements	Cr	Mo	Si	V	C	Mn	P	S	Fe
Reference wt %	4.8–5.5	1.1–1.7	0.8–1.2	0.8–1.2	0.3–0.45	0.2–0.6	Max. 0.03	Max. 0.03	Balance

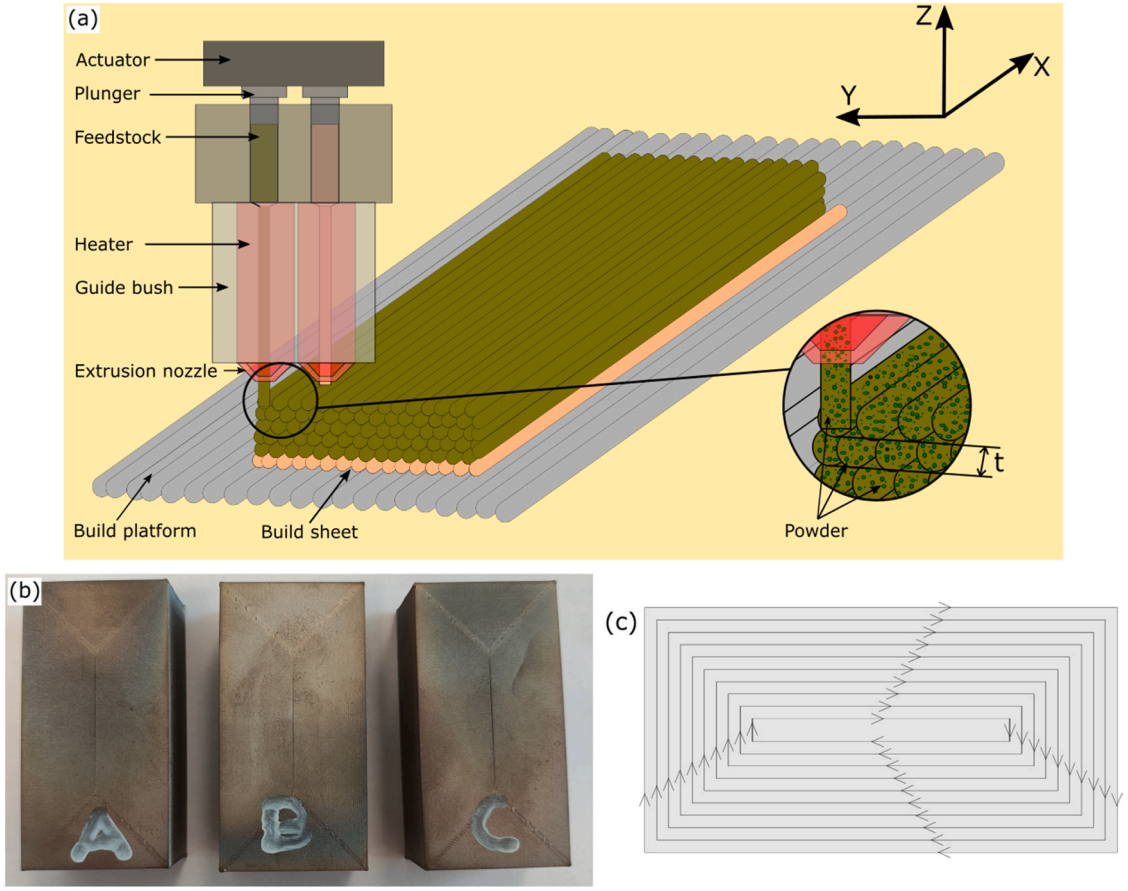

Fig. 1. (a) Building process of the MEX green body, the block samples used for the machinability tests named A, B, and C (b), and (c) the alternating line strategy pattern used during the sample production.

Table 2
Process parameters utilized for the building of H13 TS metal block samples.

Infill (%)	Printing temperature (°C)	Printing speed s (mm.s^{-1})	Layer thickness t (mm)	Hatch spacing h (mm)
100	175	30	0.15	0.48

Table 3
Parameters which were constant during the experiment.

End mill diameter (mm)	Number of teeth (–)	Depth of cut a_p (mm)	Radial depth of cut a_e (mm)	Type of milling (–)
3	4	0.2	2.4	Down milling

axis. The data were recorded with a frequency of 4 kHz and subsequently processed withDynoWare. The forces (F_x, F_y, and F_z) were evaluated within each test, which lasted a certain time and changed according to the cutting condition. The time was different in all tests, but the cutting length was always the same. The total machined length for each tool was 3420 mm. The first region (marked 1 in Fig. 2a) shows the beginning of the test, while region 7 depicts the end of the test.

Microhardness measurement (M) was performed on the LECO 247 (INNOVATEST, Prague, Czech Republic) device in an as-built state using a 50 g load and a dwell time was set to 10 s. The microhardness measurement was performed according to the methodology shown in Fig. 2a. Each evaluated line presents the microhardness evolution which serves for as an observation of the subsurface hardening effect. The structure (S) was observed within each sample in the region shown in Fig. 2a with the Olympus DSX 500 optical microscope (Olympus, Prague, Czech Republic). The detailed structure observation was performed on the samples after the machinability test, which was prepared by the puck casting, automatic polishing, and etching by 2 % nital solution was examined. Tescan Lyra 3 (Tescan, Brno, Czech Republic) with the EBSD detector was used for a detailed study of the microstructure. The scanning step for the EBSD (electron-backscatter) scanning was set to 0.19 μm. A surface quality (Q) analysis was conducted in the areas marked A to F. Parameter of the average surface roughness Ra was evaluated in each area using the T4 contour graph device. A closer surface observation was carried out with the Alicona Infinite Focus G5 digital device (Bruker, Graz, Austria) and the KEYENCE VHX F microscope (KEYENCE, Mechelen, Belgium). The surface layer was examined regarding residual stresses with RTX (Bruker, Graz, Austria).

3. Results and discussions

3.1. MEX manufactured samples characterization

The principle of the MEX method is based on the joining of material into the individual layers, which are deposited layer upon layer until the entire part is fabricated. The top surface directly after the printing is depicted in Fig. 3a, while the side view is shown in Fig. 3b. The individual tracks corresponding to the hatch spacing are visible. The surface roughness evaluated with the KEYENCE digital microscope is depicted in Fig. 3c and d (top and side surface respectively). The surface quality of as-built samples (Ra 6.45 μm, Rz 24.3 μm) does not comply with the near net shape that is used for the parts in industry. Due to this reason, post-processing milling machining was necessary [29].

Table 4
Individual tests prepared and visualized by the full factorial DoE.

Test	v_c (m.min^{-1})	f_z (mm)	Cooling conditions	Sample
I	90	0.0075	FC	A
II	80	0.005	FC	
III	90	0.0075	DM	
IV	100	0.01	FC	
V	80	0.005	DM	B
VI	100	0.01	DM	
VII	90	0.0075	DM	
VIII	90	0.0075	FC	
IX	100	0.005	FC	C
X	100	0.005	DM	
XI	80	0.01	DM	
XII	80	0.01	FC	

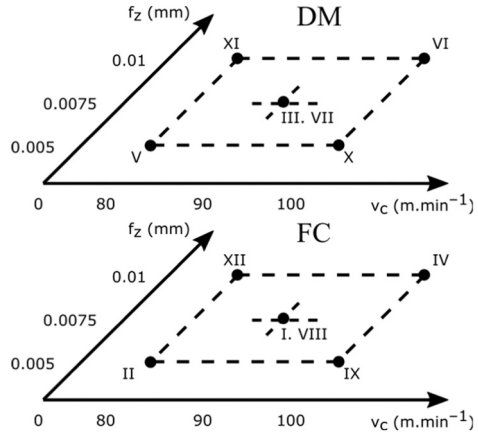

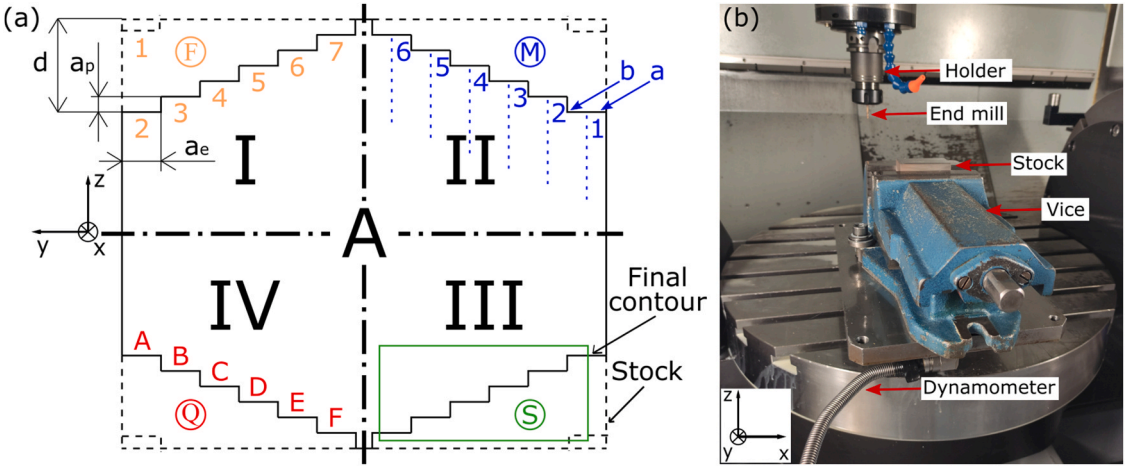

Fig. 2. (a) Detail of the used methodology showing the areas of the forces measurement (F), microhardness evaluation (M), structure observation (S), and quality examination (Q). Each variable was evaluated for each test and (b) the real setup of the experiment during the machinability tests.

The top surface depicted in Fig. 3a contains a visible crack (identified by the red arrow) along the x-axis, which was caused by none of the deposited feedstock in this area (corresponding with the applied 3D printing strategy depicted in Fig. 1c). The paths related to the hatch spacing are visible on the cover surface as well as the height (layer thickness) of the individual layers on the site of the sample (see Fig. 3b). The surface also consists of numerous pores (marked with the yellow arrows shown in Fig. 3c) that originated during the 3D printing process. Fig. 3d shows the Rz surface analysis, which could play a significant role during machining of this cover layer. These aspects led to the subtractive shaping of both sites (top and site), which brought about an accuracy of the sample already prepared for testing.

3.2. Tool wear evaluation

Tool wear (TW) was monitored using the optical microscope. The TW of the cutting tips was evaluated as the distance between the tool cutting edge and the end of the reached TW. Fig. 4a depicts the top view of the endmill and Fig. 4b presents a detail of the tip of the worn end mill at the end of the cutting test. The TW observed on the cutting tips, which was measured at the end of the test, is shown in Fig. 4c. The point in the graph characterizes the average TW (calculated from the four measured tips) as well and the deviation is presented as the highest and the lowest measured TW. The TW increase was observed with the higher feed per tooth (see tests III, V, and VI). All these tests were carried out under the DM, which resulted in lower TW in comparison to the FC. Considering the TW deviation (difference in obtained TW between each cutting tip within the end mill), it featured an increasing tendency with the increasing feed per tooth. The tests, which were performed under the same feed per tooth but with different cutting speeds resulted, in higher TW in the case of the higher cutting speed. This fact proved that the final TW was dominantly affected by the feed per tooth as well as by the cutting speed (similar to Niancong et al. [30]). The DM (within the tests performed under the same cutting condition) brought about lower TW and lower deviation. The lowest observed TW was reached in test V (the lowest cutting speed, feed per tooth, and DM). In this case, the average TW reached 0.12 mm after 3420-mm cutting length and 20.1 minutes in cut (the longest performed cutting time) and featured the lowest TW deviation. The opposite result was obtained in test IV (the highest cutting conditions and FC) where the average TW exhibited 0.29 mm after

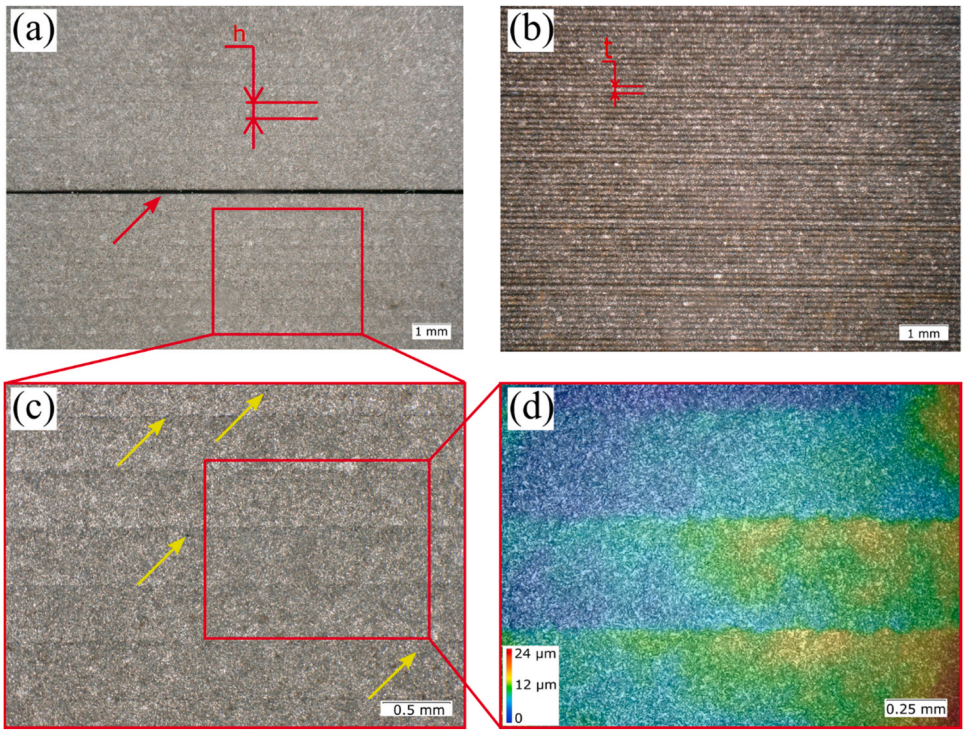

Fig. 3. (a) Top surface directly after the printing, (b) side view in as-built state, (c) area of interest, and (d) Rz surface roughness analysis.

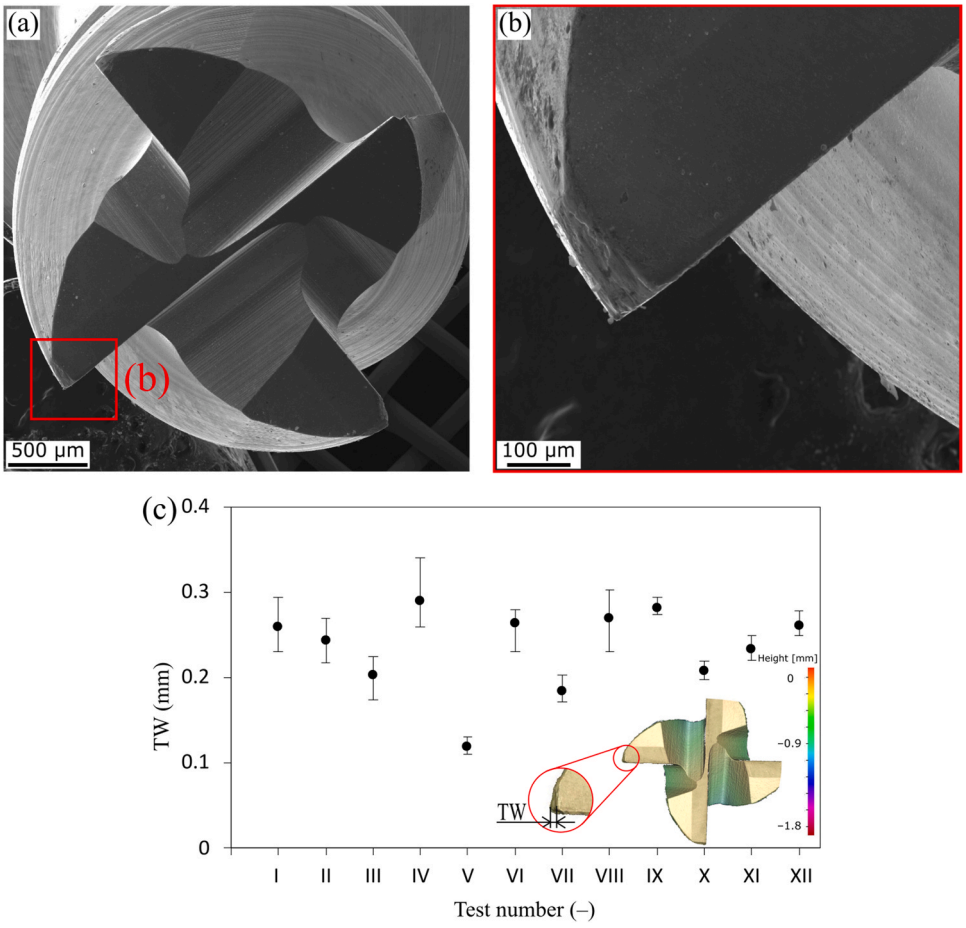

Fig. 4. SEM images of used end mill: (a) front view, (b) detail of the cutting tip displayed in (a), and (c) TW evaluated for each cutting tip depicted for individual tests.

3420 mm cutting length and 8 minutes in cut (the lowest performed cutting time). In addition, the deviation exhibited the highest observed value.

3.3. Cutting forces evaluation

In this work, the cutting forces, i.e., F_x, F_y, and F_z, are presented since the F_y force reached the highest value during the milling operation. The testing procedure was carried out according to Table 4, while the forces were recorded by the Dynoware program, subsequently calculated as an average force value (using the same program), and exported out of the program. This process reduced the effect of frequent errors, for example noises. Therefore, the calculated forces are presented as average values related to the single region corresponding to each test.

The dependences of the average F_x, F_y, and F_z forces on the cutting length under FC and DM are depicted in Fig. 5. The dominant force (the highest observed average values) is created along the y-axis, which corresponds to the feed direction, but the lowest values were monitored in the vertical direction (z-axis); these are related to the passive force generated during the machining. The obtained data were interpolated with regression lines, which exhibited an increasing tendency (the forces increased with the rising cutting length) in the case of the cutting tests carried out under FC, while DM brought about a stable and balanced course of the forces. There was not any visible deviation from the regression lines except test IV where the highest deviation was observed. This test featured the highest cutting conditions with applied cooling of the tool. Test XII featured the steepest observed tendency among the tests. The difference between the first and the last measurement was

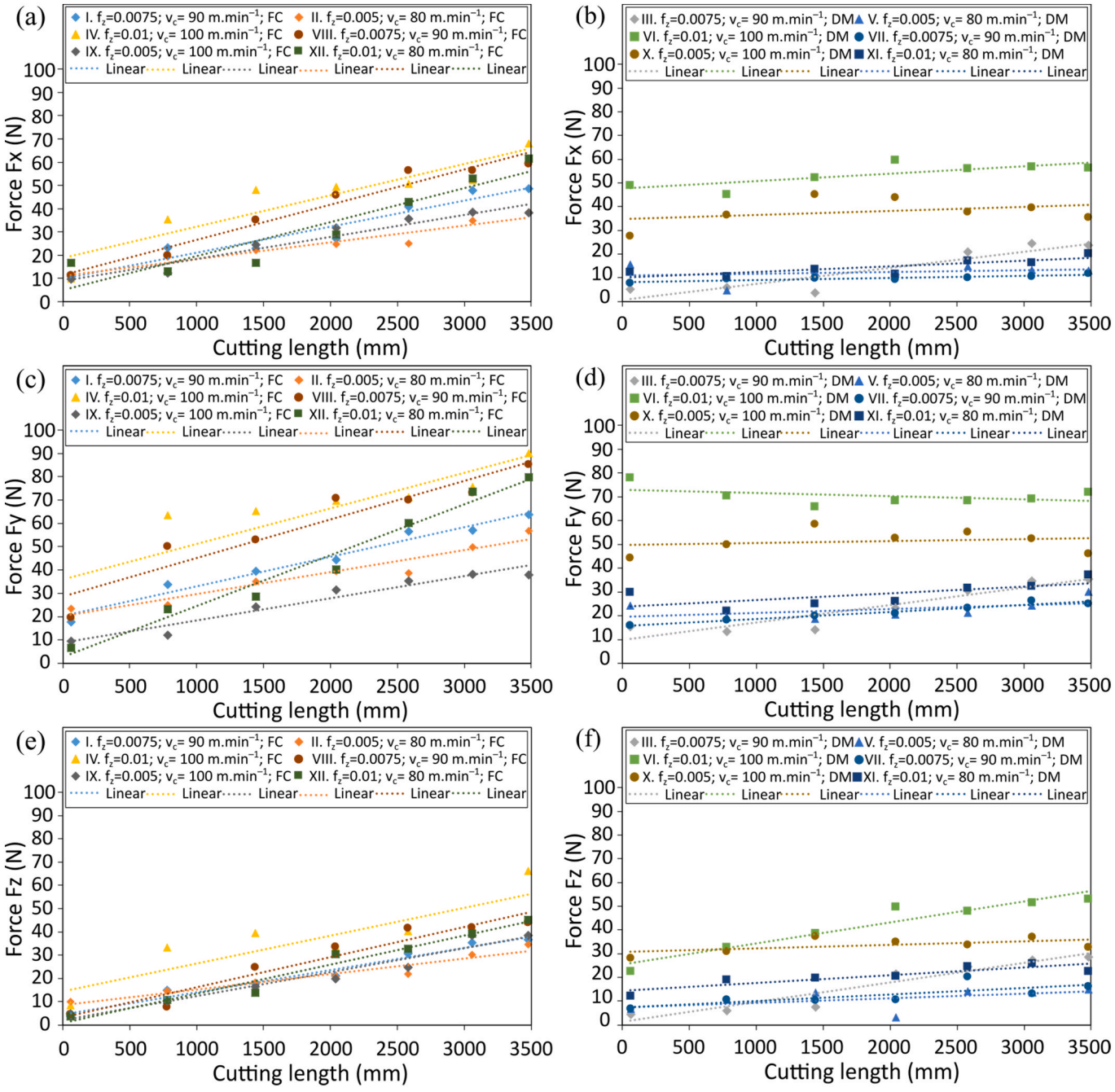

Fig. 5. Dependence of the average F_x, F_y, and F_z forces on cutting length, (a) F_x force under the FC, (b) F_x force under the DM, (c) F_y force under the FC, (d) F_y force under the DM, (e) F_z force under the FC, (f) F_x force under the DM.

73.3 N, which was the highest observed difference. This effect could have been caused by the lowest cutting speed and feed per tooth, which caused the longest cutting time (20.1 min). At the beginning of the test (new tool), the observed F_y force was at the minimum value compared to the other tests, but at the end, the average value increased to values similar to those in tests IV and VIII (carried out under the higher cutting speeds and feed per tooth).

For better visualization, the graphs were plotted separately for the tests performed under FC (see Fig. 5a, c, and e) as well as DM (see Fig. 5b, d, and f). The difference between FC and DM is visible (the increasing tendency in the case of FC and stable and balance progress for the DM). The tests under DM exhibited lower average forces (the cutting speeds of 90 m.min^{-1} and 80 m.min^{-1}) in comparison to the tests under FC. The highest average forces were observed in test IV. The forces measured in region 1 (corresponding to Fig. 2a) were similar to those in the other tests, but in region 2 a rapid increase was noticed. The increase was entailed by the rapid TW which occurred at the beginning of the test and propagated with the cutting length. Generally, higher cutting speed generates lower forces [31,32], which was confirmed in in test IX where the cutting speed was set to 100 m.min^{-1} and the F_y force exhibited the lowest observed value. Not only the cutting speed but also the lowest feed per tooth (0.005 mm) reduced the cutting forces. It can be concluded that the feed per tooth affected the cutting forces. The end mill is exposed to a higher load corresponding to the higher feed per tooth, which can cause sudden TW resulting in the rapid increase of forces as mentioned above. In addition, the higher cutting forces can also increase surface roughness [33]. The milling operation is characterized by an intermittent cut, which can be described as a load period (in the cut) alternating with a load-free period (out of the cut). The tool life can be affected by this aspect. Tools can be weakened by a thermal shock, which is a sudden temperature change. This is more harmful to tool life than just an exposure to high temperatures [34], which is a vast difference when compared to the TW during technologies with continuous cut [35]. The tool, which is exposed to thermal shocks during interrupted cutting can create thermal fatigue, which can result in thermal cracks [36]. When the tool gets in touch with the workpiece and starts to cut, it creates friction which causes the temperature to rise. However, when the cutting is complete and the edge is removed from the workpiece, coolant is immediately applied to cool it down. Once cooled, the edge is quickly put back into the cutting operation and heats up again. The effect of cooling was well seen during the experiment. Since the tool was not cooled down during the cutting, the cutting forces exhibited a more stable course resulting in better surface quality (represented with Ra parameter) and lower TW described in the previous section.

3.4. Quality of the machined surface evaluation

The average surface roughness characterized by the Ra parameter was evaluated as described in Fig. 2a. Fig. 6 presents the influence of the cutting length on Ra, whereas Fig. 6a represents the tests, which exhibited a stable or decreasing tendency of Ra on the cutting length, and Fig. 6b is characterized by an increasing roughness primarily at the end of the cutting length. DM exhibited lower surface roughness in all tests in comparison to FC. After analyzing the data, it can be concluded that the increasing feed per tooth resulted in higher surface roughness (the same increasing tendency was examined by Oliveira et al. [37] and Zhirong et al. [38]), but in the test VII (middle cutting conditions, i.e., v_c = 90 m.min^{-1} and f_z = 0.0075 mm), the surface roughness reached the minimum value of 0.08 μm. In other words, the surface roughness is influenced by the feed per tooth and the type of cooling since the cutting speed resulted in very similar Ra values in tests with the same f_z and FC. The FC caused higher surface roughness of 0.13 μm in the test IV. With the lower cutting speed, the lower surface roughness can be reached.

The surface texture was studied in test VII which reached the lowest surface roughness. Fig. 7a shows the scan of the cutting lengths from the top view. The detail of individual tracks A to F is depicted in Fig. 7b. It can be seen how burrs occurring on the edge increased with the cutting length. The burrs at track F (the biggest observed burrs) are marked with yellow arrows and the SEM detail is also included. The higher burr propagation tendency is accompanied by the TW evolution (the same conclusion was developed by Aslantas and Alatrushi [39]). As the TW propagated, the chip did not form along the edge of the cutting length. The down milling was performed during the testing, which can lead to higher burr width on the edge of the workpiece in comparison to up milling [40]. The detail of the induced oscillation during the lead-out (visualized with the blue area) of the tool is depicted in Fig. 7c. Furthermore, the higher the cutting speed, the higher the vibration amplitude, which can impart higher surface roughness [41]. In other words, the lower cutting forces (as in the test VII) can lead to lower elastoplastic deformation during the cutting process, which can result in improved surface roughness [42]. Fig. 7d shows a detail of the surface texture of the milling paths corresponding with the feed per tooth. The adhered chips are highlighted with black arrows.

3.5. Statistic

To analyze measurements of the surface quality and the cutting forces, standard tools of regression analysis were used. The significance level considered for all hypotheses testing was set to 5 %. All regression models were required to be hierarchical (if there was a statistically significant effect of interaction using a factor, then the linear effect of this factor is presented in the model even if it is not statistically significant). Used full factorial DoE enabled a fitting of the model with linear effects of all the observed factors, their interactions, covariate effect (machined distance), and the test for a presence of statistically significant curvature of the response surface by DoE's central points.

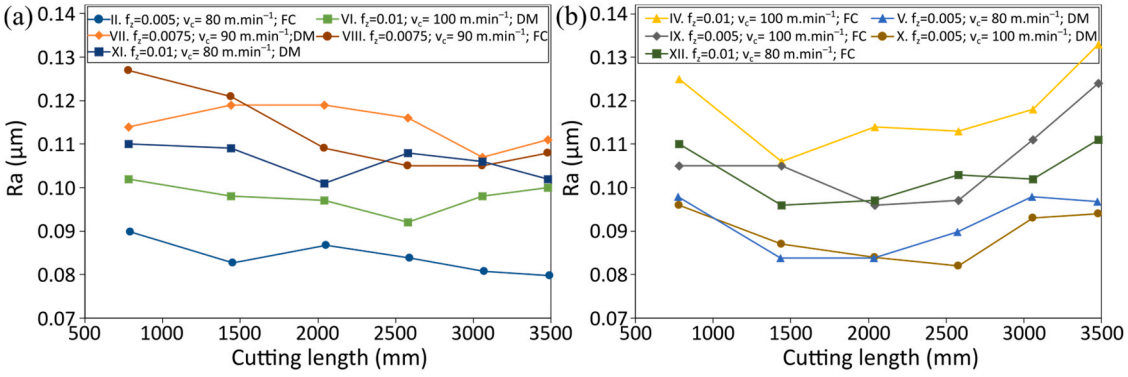

Fig. 6. Surface quality represented with average surface roughness parameter Ra influenced by the cutting lengths depicted for different tests, (a) tests II, V, VI, VIII, and XI and (b) tests IV, VII, IX, X, XII.

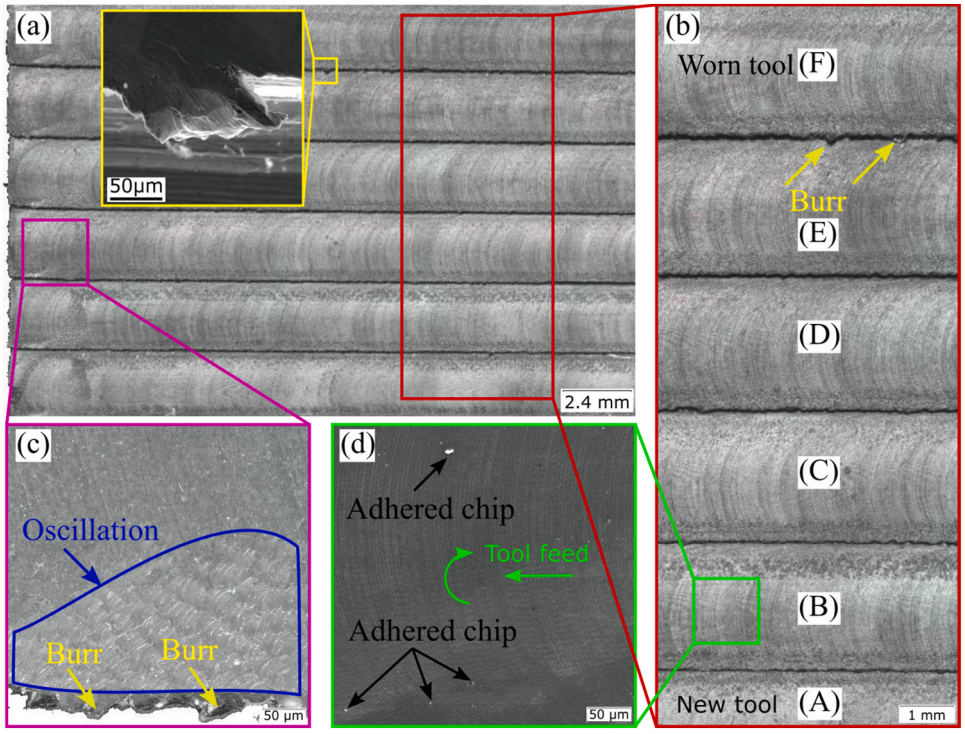

Fig. 7. Surface texture obtained in test VII: (a) scan of the cutting lengths, (b) detail of the individual tracks A to F, (c) the detail of the induced oscillation during the lead out of the tool, and (d) the detail of the surface texture depicting the milling traces corresponding with the feed per tooth.

3.5.1. Surface quality statistical evaluation

The resulting regression for the surface quality (Ra parameter) can be seen in Eq. 1a and b, where the Eq. 1a represents the regression model under FC, while Eq. 1b is linked to DM.

$$Ra = 0.09392 + 2.333 \bullet f_z \quad [\mu m] \tag{1a}$$

$$Ra = 0.07514 + 2.333 \bullet f_z \quad [\mu m] \tag{1b}$$

The coefficient of determination (R^2) of this model is 64.26 %. This means that 64.26 % of the total variability of Ra can be explained by only these two significant factors. Another inference from the same equation is that the optimal setting for minimizing Ra is low feed per tooth (0.005 mm) under DM. The value of Ra predicted for this setting is 0.08 µm with a 95 % prediction interval for Ra (0.0704225, 0.103189). T-values and P-values of significant factors in the Ra regression model corresponding to feed per tooth are 5.04 and 0.00 for DM and –9.93 and 0.00 for FC. Based on the T-values, it can be seen that the impact of cooling on Ra is higher than the effect of feed per tooth. The remaining measured factors and their interactions were removed from the model due to having statistically insignificant effects on Ra. Similarly, the effects of covariate (machined distance) and curvature were not statistically significant. Since the effect of the cutting length (and other factors) was low enough, aggregating data over insignificant predictions can allow a performance of a lack of fit test for model adequacy. The P-value corresponding to this test is 0.444, which means that there is not enough evidence that the computed model is not adequate to fit the data.

3.5.2. Cutting forces statistical evaluation

Regression analysis for cutting forces contains only statistically significant parameters, which can be seen in Eq. 2a and b corresponding to force Fx under FC and DM respectively. Eq. 3a and b is attributed to the Fy force under FC and DM and Eq. 4a (FC) and b (DM) characterizes the

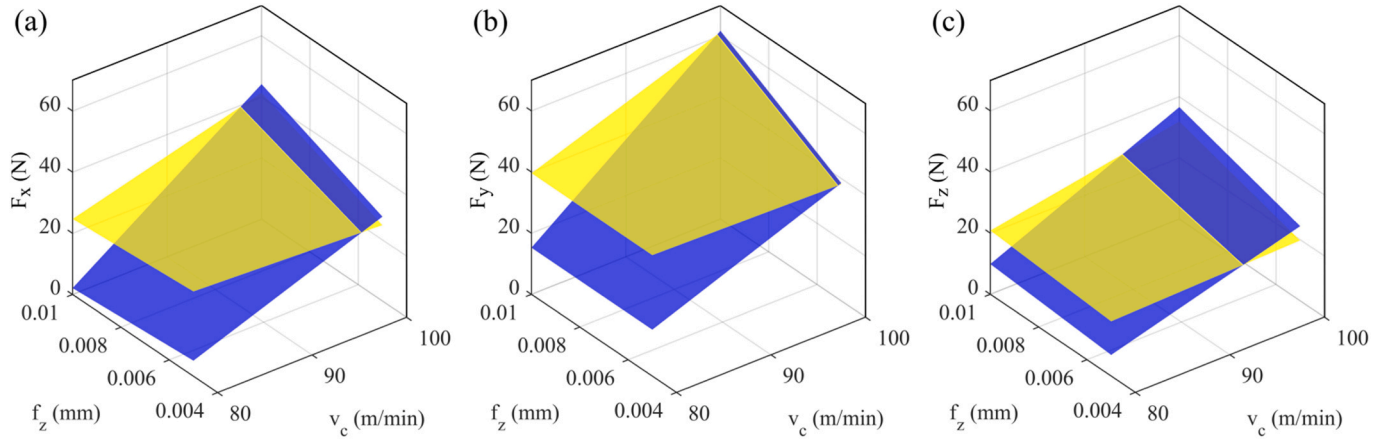

Fig. 8. Graphical visualization of the cutting forces equations, where the yellow plane characterizes the FC and the blue plane the DM, (a) characterization of the Eq. 2a and b, (b) Eq. 3a and b, and (c) Eq. 4a and b.

Fz force. Fig. 8 shows the graphical visualization of equations 2 – 4, where the yellow plane characterizes the FC and the blue plane the DM. Based on the statistically obtained data, it can be stated that the higher cutting speed under FC decreased the cutting forces in comparison to the lower cutting speed.

$$F_x = 106.0 - 16277 \bullet f_z - 1.126 \bullet v_c + 0.007236 \bullet \text{cutting length} + 196 \bullet f_z \bullet v_c \quad [N] \tag{2a}$$

$$F_x = -18.3 - 16277 \bullet f_z - 1.145 \bullet v_c + 0.007236 \bullet \text{cutting length} + 196 \bullet f_z \bullet v_c \quad [N] \tag{2b}$$

$$F_y = 119.9 - 18390 \bullet f_z - 1.222 \bullet v_c + 0.00848 \bullet \text{cutting length} + 230.1 \bullet f_z \bullet v_c \quad [N] \tag{3a}$$

$$F_y = -3.5 - 18390 \bullet f_z + 0.016 \bullet v_c + 0.00848 \bullet \text{cutting length} + 230.1 \bullet f_z \bullet v_c \quad [N] \tag{3b}$$

$$F_z = 28.9 - 6768 \bullet f_z - 0.368 \bullet v_c + 0.007547 \bullet \text{cutting length} + 92.1 \bullet f_z \bullet v_c \quad [N] \tag{4a}$$

$$F_z = -44.7 - 6768 \bullet f_z + 0.415 \bullet v_c + 0.007547 \bullet \text{cutting length} + 92.1 \bullet f_z \bullet v_c \quad [N] \tag{4b}$$

The coefficients of determination of the computed models are 72.43 % for F_x, 68.06 % for F_y, and 75.32 % for F_z. A positive fact is that all regression models for cutting forces are very similar because of the same direction of signs. P-Values correspond to used regression coefficients, which are summarized in Table 5. Unfortunately, this time neither covariate nor curvature can be considered statistically insignificant. Significant curvature (CenterPt) means that in order to find a truly adequate model of cutting forces, at least the quadratic effects need to be considered, but our factorial DoE cannot support these predictions (all quadratic effects in factorial DoE are aligned together).

3.6. Microhardness evaluation

Microhardness was evaluated according to the procedure depicted in Fig. 2a on the sample B (tests V–VIII), which comprised tests with the lowest as well as the highest cutting conditions. Fig. 9a shows microhardness measured on the sample surface after testing on each plane 1–6. Test V, which was carried out under the lowest cutting conditions, exhibited the lowest surface microhardness. On the other hand, test VI featured higher microhardness, especially in planes 1 and 6. Considering the cooling conditions, test VII (DM) featured higher microhardness at the beginning of the test (corresponds to plane 1–3) compared to test VIII while at the end the higher microhardness was observed in test VIII (FC). Fig. 9b depicts the course of the hardening effect attributed to line 1 (shown in Fig. 2) which featured a decreasing tendency with the higher distance from the machine surface. The microhardness is affected by the actual measured place, i.e., if the place contains residual martensite, the higher microhardness can be expected; by contrast, a pore or a defect can impart lower evaluated microhardness.

3.7. Structure observation

Fig. 10 shows light optical microscopy images taken (corresponding with Fig. 2a) from sample B subjected to machinability testing. The images present a transverse cross-section (perpendicular to the machined paths) parallel to the building direction. The structure directly under the machined surface featured a hardened layer (marked with red arrows, see Fig. 10a) affecting the surface microhardness. The layer width was approximately 20 μm, which is higher than in the case of machining the AM TiAL4V alloy [43]. The structure contains numerous pores (see Fig. 10b and c), which were created during the sintering process. Pores can be reduced using a higher sintering temperature [44] (the higher the sintering temperature, the lower porosity, and the higher density) or a lower layer thickness parameter [45]. The microstructure comprises prior austenite grains (PAGs, see Fig. 10d, blue line) with boundaries showing a different etching contrast compared to the bulk of the grains.

Fig. 11a shows a structure obtained by SEM, which consists of many pores (black spots) due to a low sintering temperature (a similar effect was observed by Li et al. [45]). The structure exhibited a martensitic structure in a prior austenite grain, which affected the machinability of H13 TS. EBSD orientation image maps (OIMs) were obtained from the vertical (YZ plane, corresponding with Fig. 2a) direction. In the OIMs, the individual grains are characterized by colors with respect to their individual orientations attributed to the Miller indices, which are depicted in the top right corner of the figure (legend triangle). Orientations of the grains were examined perpendicularly to the building direction. To clarify, the transversal scans (YZ plane) were observed perpendicularly to the x-axis (⊥x).

Structures after each test were observed, but only test V (the lowest cutting conditions) is visualized in Fig. 11. PAGs are highlighted with a black dashed line (see Fig. 11b). They consist of martensitic structure (similar results were obtained by Huang et al. [46]) tending to form in a preferential orientation based on the PAG alignment. In other words, the AM H13 material exhibited characteristic PAGs formed before strong recrystallization caused by the sintering process consisting of a mixture of large and small grains [44]. Random colors attributed to the individual grains (from the global point of view) supposing to the presence of the random texture, which was obtained by the pole figures (PFs) texture analyses. The results for sample V are depicted as stereographic projections (see Fig. 11c). The PFs document that the maximum texture intensity was 5.18 for sample V. The average grain size calculated in the subsurface area (see histogram depicted in Fig. 11d) exhibited a lower value (20 μm^2) compared to the area in the middle of the sample (25 μm^2). It can be concluded that the machining caused a hardening effect resulting in a smaller grain size and higher surface microhardness. Fig. 11e shows the Kernel Average Misorientation (KAM) maps of the subsurface area of sample V. The KAM maps can provide a measurement of the average misorientation angle for each point compared to its nearest neighboring points. This measurement can help to determine the degree of grain deformation [47]. The depth of affected zone (DoAZ, see Fig. 11e) is characterized by residual stresses, higher microhardness, and plastic deformation, which can be distinguished by the cutting speed [43]. The dependence of DoAZ on the cutting speed is shown in Fig. 11f. Increasing cutting speed caused an increase in the DoAZ due to the higher heat generated in the cutting area, which is absorbed by the

Table 5
P-values of factors used in cutting force regression models.

	Regression	f_z	v_c	Cutting length	Cooling	CenterPt	$f_z.v_c$	v_c.cooling
F_x P–value	0.000	0.010	0.061	0.000	0.000	0.002	0.000	0.000
F_y P–value	0.000	0.001	0.035	0.000	0.000	0.012	0.001	0.000
F_z P–value	0.000	0.000	0.020	0.000	0.049	0.000	0.019	0.000

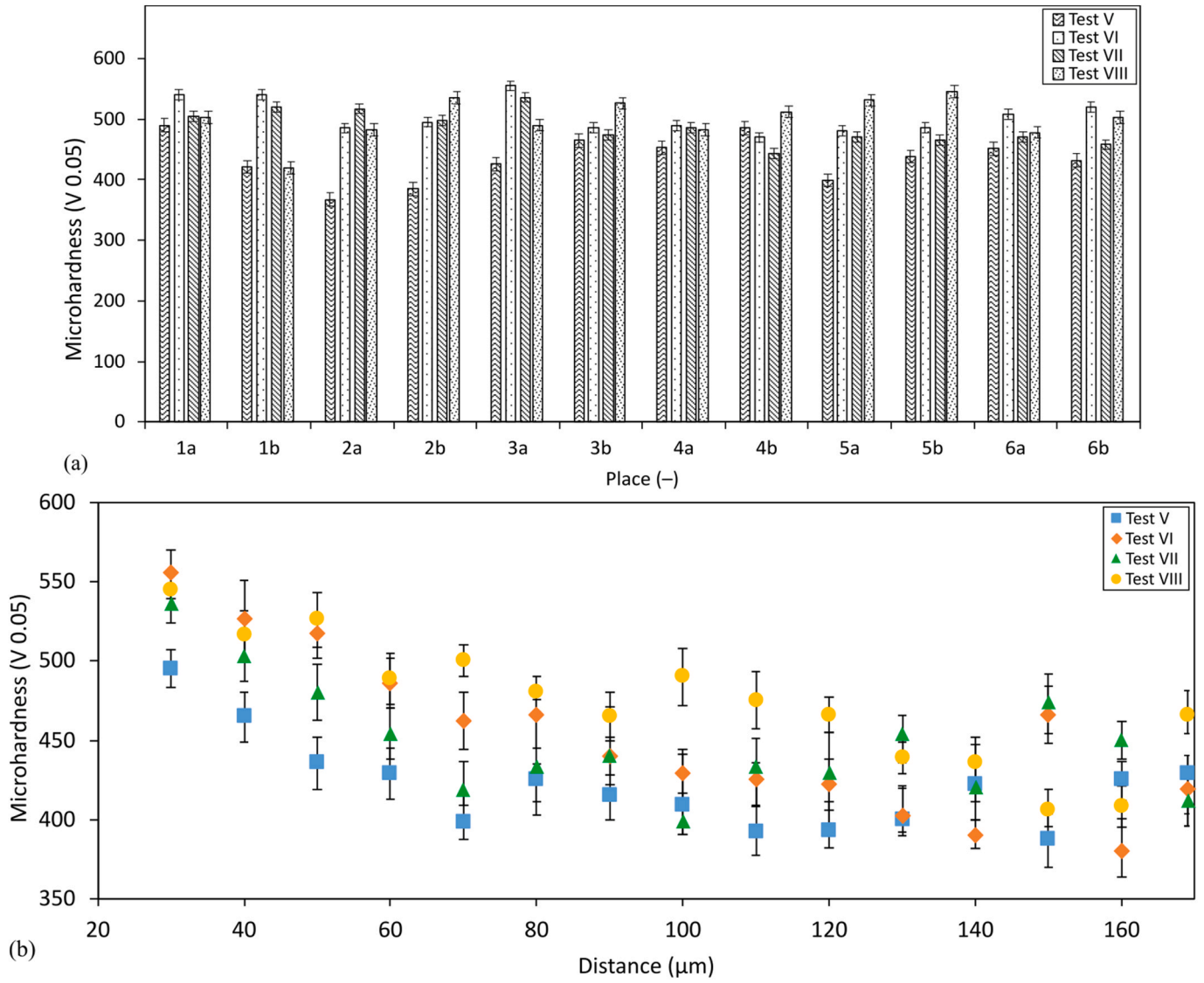

Fig. 9. (a) Surface microhardness corresponding to sample B comprising V–VIII tests, which was evaluated in two places, i.e., a and b shown in Fig. 2, and (b) dependence of the microhardness in line 1 on the distance from the machined surface.

machined surface. Furthermore, the DoAZ corresponds to the observed microhardness. This means that the higher cutting speed resulted in higher DoAZ, which can be attributed to the higher surface microhardness. Hence, test V exhibited lower surface microhardness in comparison to test VI.

3.8. Residual stresses observation

Further facts which can affect the function of the machined surface are residual stresses featuring a negative as well as positive effect. The residual stress analysis was performed by XRD, which confirmed the α phase structure of the sample, corresponding to the fully martensitic structure also revealed with EBSD. Subsequently, the last peak (see Fig. 12a, corresponding to the 25 different measurements linked to the different inclinations of the sample ensuring effective evaluation) depicted under $2\theta = 82^\circ$ was chosen as the place for the residual stresses measurement. Prior stresses σ_1 and σ_2 were calculated from the tensor consisting of normal and shear stresses, and the direction of the prior axis was visualized with the appropriate angle (see Fig. 12b). The direction corresponds to the chip formation during down milling (from the maximum to the minimum value). Hence, the more dominant chip formation regarding the residual stresses was seen in the lead-in tool phase and continued until the cutting tip reached the maximal chip area (marked with the yellow arrow) in comparison to the lead-out tool phase. In addition, the direction of the prior axis differed with cutting conditions in the range from 115° to 128°, where the highest angle was reached during test IV. Test IV exhibited the highest observed surface roughness and TW due to the highest cutting condition during the test. To analyze residual stresses, sample A was selected (consisting of test IV). This sample was chosen because when machining with a worn tool, it is more likely to have tensile residual stresses in the subsurface area in comparison to machining with a new tool [48]. This fact was not confirmed because test IV featured the highest observed compressive residual stress (prior stress σ_1 reached −83 MPa). The obtained residual stresses were influenced not only by the set cutting conditions but also with austenite-martensite transformation when manufacturing the samples [49]. With increasing cutting speed, there was a noticeable rise in plastic deformations. These deformations were observable due to the existence of materials connected to the surface, (visualized with the red arrows in Fig. 12b) [50]. Hence, the higher cutting speed increased the residual stress (σ_1, see Fig. 12c), which corresponds with the DoAZ, and surface microhardness described in the previous sections. However, the next important aspect is the feed per tooth, which entailed an increase of −40 MPa (σ_1) and −81 MPa (σ_2) in the case of test II in comparison to

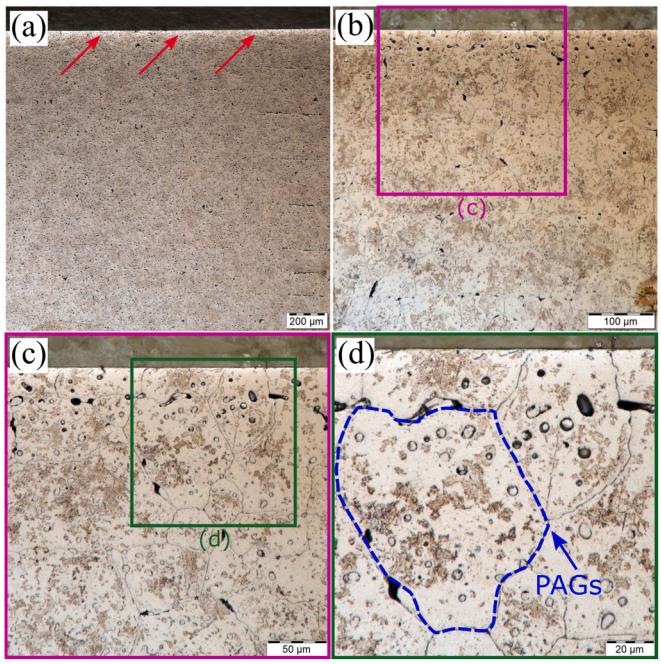

Fig. 10. Structure of H13 TS depicted directly after the machining process, (a) macro image showing a hardened surface layer, (b, c) areas of interest, and (d) detail of structure with visible PAGs.

test I. The highest observed difference was obtained for test III, where the sample featured tensile residual stress, while any other tensile residual stress was not observed. This fact can be explained by DM which imparted a higher heat transfer directly to the surface layer. This mechanism could enable a partial relaxation (due to an annealing procedure) of the residual stresses [51], which resulted in the lowest observed compressive stress (-224 MPa in prior stress σ_1 direction) as well as tensile residual stress (104 MPa in the σ_2 direction). This test corresponds to the lowest measured angle (115°) of prior stress σ_1 axis direction. In other words, it can be stated that the cooling influences the final residual stresses as well as Kara et al. found out that a cryogenic process reduced the residual stresses on the surface of the material [52, 53].

3.9. Summary

The as-built material did not feature a favorable surface quality to be considered functional surface. Based on the obtained data, the machinability of as-built H13 TS brought interesting results. Regarding TW, it was observed that the increase of feed per tooth generated higher TW. Furthermore, the tests which were carried out without cooling (DM) exhibited lower TW in comparison to FC. Generally, DM resulted in a positive effect on TW as well as on the cutting forces, which exhibited a lower and more stable course. The surface roughness evaluated with parameter Ra was improved after the machining procedure. The lower values of the Ra parameter were observed with the lower feed per tooth and DM. Not only can DM bring better results in almost all evaluated

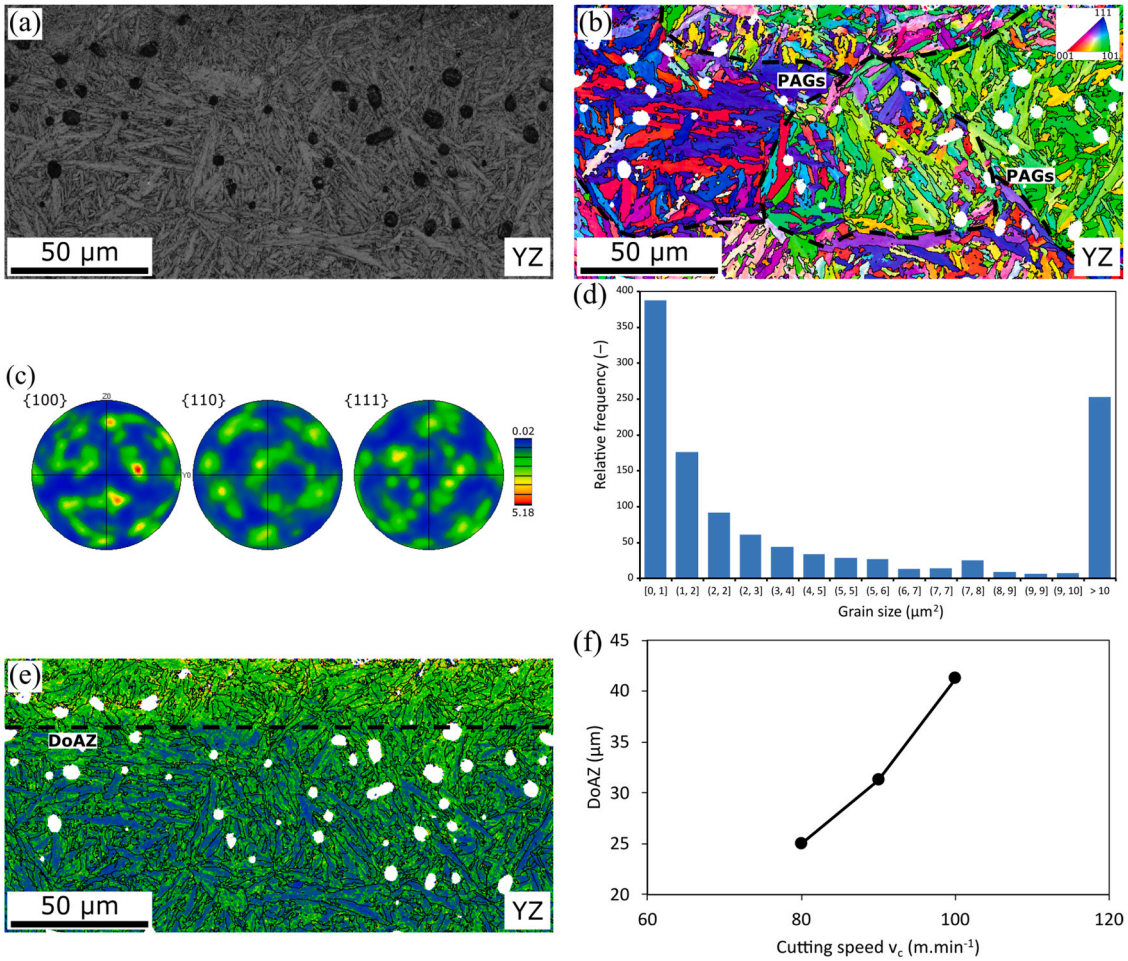

Fig. 11. (a) SEM image depicting a martensitic structure consisting of pores, (b) EBSD OIM with the PAGs in subsurface area, (c) PFs depicting texture in sample B test V, (d) the relative frequency of the grain size, (e) Kernel average misorientation maps and (f) the dependence of DoAZ on cutting speed.

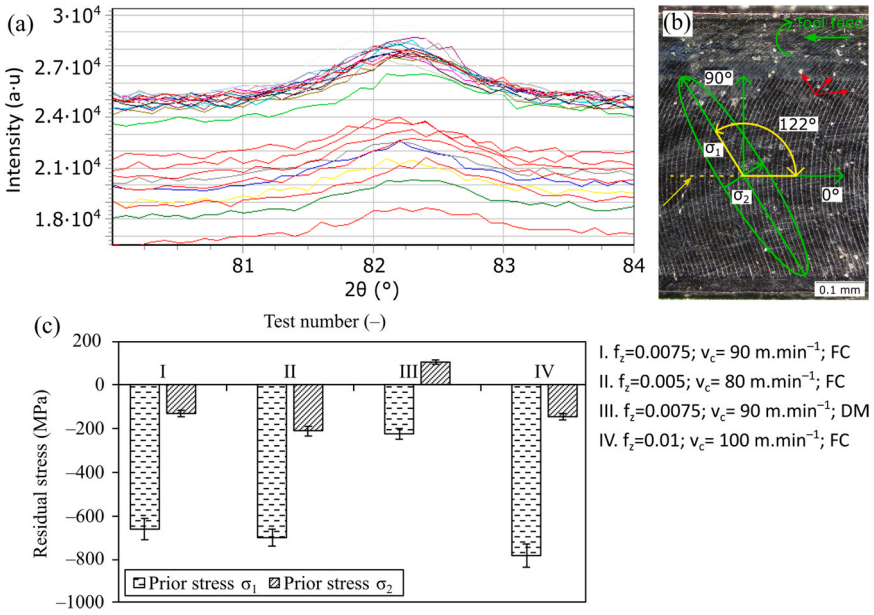

Fig. 12. XRD depicting the last peak corresponding to 25 different measurements (a), graphical visualization of the prior stress σ_1 direction (b), and (c) the residual stresses obtained for the different test numbers from the sample A.

fields, but it can also reduce production costs due to cooling savings. The final surface roughness and cutting forces can be effectively predicted by a regression model, which was examined based on the obtained data. The DoAZ featured a growing tendency with the increasing cutting speed, which influenced surface microhardness and residual stresses. The machined surface exhibited higher microhardness than the as-built one due to the lower average grain size, higher KAM parameter, and dominant existence of residual compressive stresses. Although the compressive stresses are more beneficial than the tensile ones, heat treatment would be a necessary part of the manufacturing process, which imparts a relaxation of the stresses.

One of the key challenges in MEX mold making is designing the cooling channels, which are essential for preventing the mold from overheating and ensuring the production of high-quality plastic parts. A MEX mold can be designed with conformal cooling channels that follow the contours of the mold cavity and help to improve cooling efficiency and reduce cycle time. Furthermore, the structure of the MEX material contained plenty of pores equally spread in the martensitic structure which are not favorable for the mechanical properties. Further investigation will lead to finding an effective way to reduce the final porosity with respect to the mechanical properties. Overall, MEX is a developing technology to produce industrial parts with higher durability and performance. Hence, further research has to be done.

4. Conclusion

This study has dealt with the H13 TS prepared by MEX (BMD). The main aim was to examine the effects of cutting conditions (cutting speed, feed per tooth, and cooling conditions) set according to the full factorial design of experiments on the TW, cutting forces, surface roughness, microhardness, structure, and residual stresses. A regression model was used to find the equations intended for a possible prediction of the surface roughness and the cutting forces during the manufacturing process.

The tool wear increase was observed with the higher feed per tooth. The lowest surface roughness of 0.08 μm was observed at a cutting speed of 80 m/min and a feed per tooth of 0.005 mm under FC. Additionally, the highest microhardness of 550 HV was observed at the machined surface, gradually decreasing with increasing distance from the surface. The depth of affected zone featured a 42 μm in case of the highest cutting speed 80 m/min. Under FC, the highest cutting speed, and feed per tooth the machined surface resulted in the highest compressive residual stresses of −783 MPa. Conversely, the application of DM resulted in the decrease in compressive residual stresses to −224 MPa, likely due to a partial annealing effect triggered by the heat transfer to the machined surface. Overall, the study emphasizes that DM represents a promising approach to reaching superior machined surfaces with desirable structures and residual stresses.

It is important to note that the optimal cutting conditions will vary depending on the specific part geometry and quality requirements. However, the recommendations provided in this study can serve as a starting point for optimizing the machining process. Thanks to the obtained results, the part made from MEX H13 TS (especially the injection mold or 3D printed cores) can be post-processed (by machining) more effectively with overall higher quality.

CRediT authorship contribution statement

Pavel Hrabec: Conceptualization, Formal analysis, Resources, Software, Writing – original draft. **Karel Kouril:** Conceptualization, Formal analysis, Funding acquisition, Methodology, Validation. **Stepan Kolomy:** Conceptualization, Investigation, Methodology, Validation, Visualization, Writing – original draft, Writing – review & editing. **Jan Zouhar:** Conceptualization, Methodology, Validation, Writing – original draft, Writing – review & editing. **Martin Slany:** Conceptualization, Investigation, Methodology, Supervision, Writing – original draft, Writing – review & editing. **Martin Malý:** Conceptualization, Formal analysis, Investigation, Methodology, Validation, Visualization, Writing – original draft, Writing – review & editing. **Josef Sedlak:** Conceptualization, Investigation, Methodology, Supervision, Validation, Writing – original draft, Writing – review & editing.

Declaration of Competing Interest

The authors declare that they have no known competing financial interests or personal relationships that could have appeared to influence the work reported in this paper.

Data availability

Data will be made available on request.

Acknowledgements

This research study was supported by the grant "Modern Technologies for Processing Advanced Materials Used for Interdisciplinary Applications", FSI-S-22-7957. This work has been performed in the project RICAIP: Research and Innovation Centre on Advanced Industrial Production which has received funding from the European Union's Horizon 2020 Research and Innovation Program under grant agreement No 857306 and from the Ministry of Education, Youth and Sports under OP RDE grant agreement No CZ.02.1.01/0.0/0.0/17_043/0010085.

References

[1] Z. Pitrmuc, J. Šimota, L. Beránek, P. Mikeš, V. Andronov, J. Sommer, F. Holešovský, Mechanical and Microstructural Anisotropy of Laser Powder Bed Fusion 316L Stainless Steel, Materials 15 (2022) 551, https://doi.org/10.3390/ma15020551.

[2] V. Andronov, J. Šimota, L. Beránek, J. Blažek, F. Rušar, Optimization of Process Parameters for Additively Produced Tool Steel 1.2709 with a Layer Thickness of 100 µm, Materials 14 (2021) 2852, https://doi.org/10.3390/ma14112852.

[3] Y. Liu, H. Wang, S. Li, S. Wang, W. Wang, W. Hou, Y. Hao, R. Yang, L. Zhang, Compressive and fatigue behavior of beta-type titanium porous structures fabricated by electron beam melting, Acta Mater. 126 (2017) 58–66, https://doi.org/10.1016/j.actamat.2016.12.052.

[4] J. Kranz, D. Herzog, C. Emmelmann, Design guidelines for laser additive manufacturing of lightweight structures in TiAl6V4, J. Laser Appl. 27 (2015) S14001, https://doi.org/10.2351/1.4885235.

[5] S. Kolomy, J. Sedlak, J. Zouhar, M. Slany, M. Benc, D. Dobrocky, I. Barenyi, J. Majerik, Influence of Aging Temperature on Mechanical Properties and Structure of M300 Maraging Steel Produced by Selective Laser Melting, Materials 16 (2023) 977, https://doi.org/10.3390/ma16030977.

[6] J. Sedlak, Z. Joska, J. Jansky, J. Zouhar, S. Kolomy, M. Slany, A. Svasta, J. Jirousek, Analysis of the Mechanical Properties of 3D-Printed Plastic Samples Subjected to Selected Degradation Effects, Materials 16 (2023) 3268, https://doi.org/10.3390/ma16083268.

[7] J. Gonzalez-gutierrez, S. Cano, S. Schuschnigg, C. Kukla, J. Sapkota, C. Holzer, Additive manufacturing of metallic and ceramic components by the material extrusion of highly-filled polymers: A review and future perspectives, Materials 11 (2018) 840, https://doi.org/10.3390/ma11050840.

[8] M. Strano, K. Rane, M. Farid, V. Mussi, V. Zaragoza, M. Monno, Extrusion-based additive manufacturing of forming and molding tools, Int. J. Adv. Manuf. Tech. 117 (2021) 2059–2071, https://doi.org/10.1007/s00170-021-07162-8.

[9] N. Huu, D. Toan, T. Huu, H. Thu, Effects of Infill, Infill Patterns and Number of Perimeter Shells on Casting Patterns Fabricated Using FDM Method, in: 2018 4th International Conference on Green Technology and Sustainable Development (GTSD), IEEE, 2018: pp. 207-212. ⟨https://doi.org/10.1109/GTSD.2018.8595703⟩.

[10] O. Gumus, R. Ilhan, B. Canli, Effect of Printing Temperature on Mechanical and Viscoelastic Properties of Ultra-flexible Thermoplastic Polyurethane in Material Extrusion Additive Manufacturing, J. Mater. Eng. Perform. 31 (2022) 3679–3687, https://doi.org/10.1007/s11665-021-06510-9.

[11] L. Lan, W. Wang, Z. Cui, X. Hao, Effect of scanning speed on microstructure and mechanical properties of selective laser melting AlCoCrFeNi2.1 eutectic high-entropy alloy, Mater. Lett. 330 (2023) 133321, https://doi.org/10.1016/j.matlet.2022.133321.

[12] J. Sun, Y. Zhao, L. Yang, X. Zhao, W. Qu, T. Yu, Effect of shielding gas flow rate on cladding quality of direct laser fabrication AISI 316L stainless steel, J. Manuf. Process. 48 (2019) 51–65, https://doi.org/10.1016/j.jmapro.2019.10.011.

[13] P. Parenti, D. Puccio, B. Colosimo, Q. Semeraro, A new solution for assessing the printability of 17-4 PH gyroids produced via extrusion-based metal AM, J. Manuf. Process. 74 (2022) 557–572, https://doi.org/10.1016/j.jmapro.2021.12.043.

[14] J. Vetter, F. Huber, S. Wachter, C. Körner, M. Schmidt, Development of a Material Extrusion Additive Manufacturing Process of 1.2083 steel comprising FFF Printing, Solvent and Thermal Debinding and Sintering, Procedia CIRP 113 (2022) 341–346, https://doi.org/10.1016/j.procir.2022.09.140.

[15] J. Gonzalez-gutierrez, S. Cano, S. Schuschnigg, C. Kukla, J. Sapkota, C. Holzer, Additive manufacturing of metallic and ceramic components by the material extrusion of highly-filled polymers: A review and future perspectives, Materials 11 (2018) 840, https://doi.org/10.3390/ma11050840.

[16] K. Jimbo, T. Tateno, Shape contraction in sintering of 3d objects fabricated via metal material extrusion in additive manufacturing, Int. J. Autom. Technol. 13 (2019) 354–360, https://doi.org/10.20965/ijat.2019.p0354.

[17] G. Singh, J. Missiaen, D. Bouvard, J. Chaix, Additive manufacturing of 17–4 PH steel using metal injection molding feedstock: Analysis of 3D extrusion printing, debinding and sintering, Addit. Manuf. 47 (2021) 102287, https://doi.org/10.1016/j.addma.2021.102287.

[18] M. Sæterbø, W. Solvang, Evaluating the cost competitiveness of metal additive manufacturing – A case study with metal material extrusion, CIRP J. Manuf. Sci. Technol. 45 (2023) 113–124, https://doi.org/10.1016/j.cirpj.2023.06.005.

[19] B. Breidenstein, F. Brenne, B. Denkena, T. Niendorf, B. Denkena, Effect of Post-Process Machining on Surface Properties of Additively Manufactured H13 Tool Steel, Heat Treatm. Mat. 73 (2018) 173–186, https://doi.org/10.3139/105.110359.

[20] P. Opěla, M. Benč, S. Kolomy, Z. Jakůbek, D. Beranová, High Cycle Fatigue Behaviour of 316L Stainless Steel Produced via Selective Laser Melting Method and Post Processed by Hot Rotary Swaging, Materials 16 (2023) 3400, https://doi.org/10.3390/ma16093400.

[21] F. Kara, F. Bayraktar, F. Savaş, O. Özbek1, Experimental and statistical investigation of the effect of coating type on surface roughness, cutting temperature, vibration and noise in turning of mold steel, J. Mat. Manuf. (2023) 31–43, https://doi.org/10.5281/zenodo.8020553.

[22] S. Pradhan, S. Das, P. Jena, D. Dhupal, Investigations on Surface Integrity in Hard Turning of Functionally Graded Specimen under Nano Fluid Assisted Minimum Quantity Lubrication, Adv. Mater. Process. Technol. (Abingdon, England) 8 (2022) 1714–1729, https://doi.org/10.1080/2374068X.2021.1948706.

[23] J. Chattopadhyay, R. Singh, O. Prakash, Modeling and Optimization of Surface Roughness in Hard Turning of AISI 4340 Steel with Coated Ceramic Tool. Innovation in Materials Science and Engineering, Springer Singapore Pte. Limited, Singapore, 2019, pp. 151–160, https://doi.org/10.1007/978-981-13-2944-9_15.

[24] S. Mahapatra, A. Das, Pankaj Charan, S. Das, Turning of hardened AISI H13 steel with recently developed S3P-AlTiSiN coated carbide tool using MWCNT mixed nanofluid under minimum quantity lubrication, J. Mech. Eng. Sci. (2022), https://doi.org/10.1177/09544062221126357.

[25] P. Kumar, S. Chauhan, C. Pruncu, M. Gupta, D. Pimenov, M. Mia, H. Gill, Influence of different grades of CBN inserts on cutting force and surface roughness of AISI H13 die tool steel during hard turning operation, Materials 12 (2019) 177, https://doi.org/10.3390/ma12010177.

[26] A. Çiçek, T. Kıvak, E. Ekici, F. Kara, N. Uçak, Performance of Multilayer Coated and Cryo-Treated Uncoated Tools in Machining of AISI H13 Tool Steel—Part 1: Tungsten Carbide End Mills, J. Mater. Eng. Perform. 30 (2021) 3436–3445, https://doi.org/10.1007/s11665-021-05656-w.

[27] A. Çiçek, E. Ekici, T. Kıvak, F. Kara, N. Uçak, Performance of Multilayer Coated and Cryo-treated Uncoated Tools in Machining of AISI H13 Tool Steel—Part 2: HSS End Mills, J. Mater. Eng. Perform. 30 (2021) 3446–3457, https://doi.org/10.1007/s11665-021-05657-9.

[28] F. Montevecchi, N. Grossi, H. Takagi, A. Scippa, H. Sasahara, G. Campatelli, Cutting Forces Analysis in Additive Manufactured AISI H13 Alloy, Procedia CIRP 46 (2016) 476–479, https://doi.org/10.1016/j.procir.2016.04.034.

[29] Y. Bai, C. Zhao, J. Yang, R. Hong, C. Weng, H. Wang, Microstructure and machinability of selective laser melted high-strength maraging steel with heat treatment, J. Mater. Process. Technol. 288 (2021) 116906, https://doi.org/10.1016/j.jmatprotec.2020.116906.

[30] N. Liu, C. Zheng, D. Xiang, H. Huang, J. Wang, Effect of cutting parameters on tool wear under minimum quantity cooling lubrication (MQCL) conditions, Int. J. Adv. Manuf. Tech. 105 (2019) 515–529, https://doi.org/10.1007/s00170-019-04259-z.

[31] D. Geng, Z. Sun, Y. Liu, L. Liu, E. Ying, J. Cai, X. Jiang, D. Zhang, Unravelling the influence of vibration on material removal and microstructure evolution in ultrasonic transversal vibration-assisted helical milling of Ti-6Al-4V holes, J. Mater. Process. Technol. 326 (2024) 118320, https://doi.org/10.1016/j.jmatprotec.2024.118320.

[32] Z. Sun, D. Geng, H. Guo, Q. Zhang, Y. Liu, L. Liu, X. Jiang, D. Zhang, Introducing transversal vibration in twist drilling: Material removal mechanisms and surface integrity, J. Mater. Process. Technol. 325 (2024) 118296, https://doi.org/10.1016/j.jmatprotec.2024.118296.

[33] S. Jeyakumar, K. Marimuthu, T. Ramachandran, Prediction of cutting force, tool wear and surface roughness of Al6061/SiC composite for end milling operations using RSM, J. Mech. Sci. Technol. 27 (2013) 2813–2822, https://doi.org/10.1007/s12206-013-0729-z.

[34] M. Vaziri, S. Nowruzpour Mehrian, M. Naei, J. Sheikh Ahmad, Modification of Shock Resistance for Cutting Tools Using Functionally Graded Concept in Multilayer Coating, J. Therm. Sci. Eng. Appl. 7 (2015), https://doi.org/10.1115/1.4028982.

[35] L. Pelikán, M. Slaný, O. Stránský, L. Beránek, Z. Pitrmuc, L. Čepová, Š. Dvořáčková, Novel drill geometries for dry drilling of stainless steel, J. Manuf. Process. 92 (2023) 500–520, https://doi.org/10.1016/j.jmapro.2023.03.006.

[36] Y. Kondo, S. Sakamoto, T. Fujita, M. Yamaguchi, K. Yamaguchi, K. Uehara, Effects of Cooling Conditions on Thermal Crack Initiation of Brittle Cutting Tools during Intermittent Cutting, Key Eng. Mater. 656-657 (2015) 237–242, https://doi.org/10.4028/www.scientific.net/KEM.656-657.237.

[37] A. Oliveira, A. Jardini, E. Del Conte, Effects of cutting parameters on roughness and residual stress of maraging steel specimens produced by additive manufacturing, Int. J. Adv. Manuf. Tech. 111 (2020) 2449–2459, https://doi.org/10.1007/s00170-020-06309-3.

[38] Z. Liao, A. la Monaca, J. Murray, A. Speidel, D. Ushmaev, A. Clare, D. Axinte, R. M'saoubi, Surface integrity in metal machining - Part I: Fundamentals of surface characteristics and formation mechanisms, Int. J. Mach. Tools Manuf. 162 (2021) 103687, https://doi.org/10.1016/j.ijmachtools.2020.103687.

[39] K. Aslantas, L. Alatrushi, Experimental Study on the Effect of Cutting Tool Geometry in Micro-Milling of Inconel 718, Arab. J. Sci. Eng. 46 (2011) (2021) 2327–2342, https://doi.org/10.1007/s13369-020-05034-z.

[40] S. Zaidi, N. Ul Qadir, S. Jaffery, M. Khan, M. Khan, J. Petru, Statistical Analysis of Machining Parameters on Burr Formation, Surface Roughness and Energy

Consumption during Milling of Aluminium Alloy Al 6061-T6, Materials 15 (2022) 8065, https://doi.org/10.3390/ma15228065.
[41] T. Pham, D. Nguyen, T. Banh, V. Tong, Experimental study on the chip morphology, tool–chip contact length, workpiece vibration, and surface roughness during high-speed face milling of A6061 aluminum alloy, J. Eng. Manufact. 234 (2019), https://doi.org/10.1177/0954405419863.
[42] X. Zhang, T. Yu, Y. Dai, S. Qu, J. Zhao, Energy consumption considering tool wear and optimization of cutting parameters in micro milling process, Int. J. Mech. Sci. 178 (2020) 105628, https://doi.org/10.1016/j.ijmecsci.2020.105628.
[43] U. Alves, A. Hassui, M. de Oliveira, P. Neto, C. Ventura, Microstructural and machinability aspects of electron beam melted Ti–6Al–4V with different building orientations, Prog. Addit. Manuf. 8 (2023) 131–141, https://doi.org/10.1007/s40964-022-00317-3.
[44] P. Nandwana, R. Kannan, D. Siddel, Microstructure evolution during binder jet additive manufacturing of H13 tool steel, Addit. Manuf. 36 (2020) 101534, https://doi.org/10.1016/j.addma.2020.101534.
[45] S. Li, H. Deng, X. Lan, B. He, X. Li, Z. Wang, Developing cost-effective indirect manufacturing of H13 steel from extrusion-printing to post-processing, Addit. Manuf. 62 (2023) 103384, https://doi.org/10.1016/j.addma.2022.103384.
[46] G. Huang, K. Wei, X. Zeng, Microstructure and mechanical properties of H13 tool steel fabricated by high power laser powder bed fusion, Mater. Sci. Eng. A, Struct. Mater.: Prop. Micro. Process. 858 (2022) 144154, https://doi.org/10.1016/j.msea.2022.144154.
[47] Y. Qi, Z. Hu, H. Zhang, X. Nie, C. Zhang, H. Zhu, High strength Al–Li alloy development for laser powder bed fusion, Addit. Manuf. 47 (2021) 102249, https://doi.org/10.1016/j.addma.2021.102249.
[48] G. Byrne, D. Dornfeld, B. Denkena, Advancing Cutting Technology, CIRP Ann. 52 (2003) 483–507, https://doi.org/10.1016/S0007-8506(07)60200-5.
[49] P. Mercelis, J. Kruth, Residual stresses in selective laser sintering and selective laser melting, Rapid Prototyp. J. 12 (2006) 254–265, https://doi.org/10.1108/13552540610707013.
[50] S. Jeelani, K. Ramakrishnan, Surface damage in machining titanium 6Al-2Sn-4Zr-2Mo alloy, J. Mater. Sci. 20 (1985) 3245–3252, https://doi.org/10.1007/BF00545191.
[51] H. Holzapfel, V. Schulze, O. Vöhringer, E. Macherauch, Residual stress relaxation in an AISI 4140 steel due to quasistatic and cyclic loading at higher temperatures, Mater. Sci. Eng. A, Struct. Mater.: Prop. Micro. Process. 248 (1998) 9–18, https://doi.org/10.1016/S0921-5093(98)00522-X.
[52] F. Kara, A. Çiçek, H. Demir, Effect of Deep Cryogenic Treatment on Microstructure, Mechanical Properties, and Residual Stress of AISI 52100 Bearing Steel, Eng. Sci. (2023), https://doi.org/10.30919/es960.
[53] F. Kara, O. Özbek, N. Özbek, İ. Uygur, Investigation of the Effect of Deep Cryogenic Process on Residual Stress and Residual Austenite, Gazi J. Eng. Sci. (2) (2021) 143–151, https://doi.org/10.30855/gmbd.2021.02.07.